

VLA 1.4 GHz CATALOGS OF THE ABELL 370 AND ABELL 2390 CLUSTER FIELDS

ISAK G. B. WOLD¹, FRAZER N. OWEN², WEI-HAO WANG³, AMY J. BARGER^{1,4,5}, AND RYAN C. KEENAN¹

Draft version August 5, 2021

ABSTRACT

We present 1.4 GHz catalogs for the cluster fields Abell 370 and Abell 2390 observed with the Very Large Array. These are two of the deepest radio images of cluster fields ever taken. The Abell 370 image covers an area of $40' \times 40'$ with a synthesized beam of $\sim 1.7''$ and a noise level of $\sim 5.7 \mu\text{Jy}$ near field center. The Abell 2390 image covers an area of $34' \times 34'$ with a synthesized beam of $\sim 1.4''$ and a noise level of $\sim 5.6 \mu\text{Jy}$ near field center. We catalog 200 redshifts for the Abell 370 field. We construct differential number counts for the central regions (radius $< 16'$) of both clusters. We find that the faint ($S_{1.4 \text{ GHz}} < 3 \text{ mJy}$) counts of Abell 370 are roughly consistent with the highest blank field number counts, while the faint number counts of Abell 2390 are roughly consistent with the lowest blank field number counts. Our analyses indicate that the number counts are primarily from field radio galaxies. We suggest that the disagreement of our number counts can be largely attributed to cosmic variance.

Subject headings: cosmology: observations

1. INTRODUCTION

Radio surveys probe active galactic nuclei (AGNs) and star-forming (SF) galaxies. SF galaxies produce non-thermal radio continuum through synchrotron emission from supernova remnants. For these sources, the 1.4 GHz luminosity is found to be an accurate indicator of the star formation rate (Condon 1992). AGNs also emit synchrotron radiation, which is ultimately powered by accretion onto supermassive black holes (SMBHs). Observed tight correlations between SMBH mass and bulge properties (Kormendy & Richstone 1995; Ferrarese & Merritt 2000; Tremaine et al. 2002) plus various theoretical considerations (Granato et al. 2004; Croton et al. 2006; Bower et al. 2006) have led to the hypothesis that AGNs regulate star formation. Thus, radio surveys are an important tool to constrain how stars and SMBHs evolve and interact as a function of cosmic time.

There is still debate over the faint radio population, especially regarding the differential source counts. AGNs are found to dominate the counts at high flux densities, while SF galaxies are thought to emerge at lower flux densities (Condon 1989). However, the exact composition — and the counts themselves — are debated below $S_{1.4 \text{ GHz}} = 100 \mu\text{Jy}$. The disagreement in faint radio counts from one survey to the next has been attributed mostly to instrumental and analysis effects, not to cosmic variance (Condon 2007). For example, for the heavily studied Hubble Deep Field-North (HDF-N), three different groups have derived faint-end number counts, with each subsequent study finding them to be incrementally

higher (Richards 2000; Biggs & Ivison 2006; Morrison et al. 2010). However, studies such as Biggs & Ivison (2006), which present catalogs for three deep radio fields, have shown that similar instrument configurations and analysis methods still result in faint counts that are inconsistent with merely Poisson variation. It is important to obtain as many deep radio images as possible to help resolve this issue, especially since cosmic variance could be an important factor.

In this paper, we present deep radio observations of two heavily-studied cluster fields. Radio surveys of cluster fields have been vital to many areas of study. For example, they have improved our understanding of cluster members by finding evidence for a population of dust-obscured SF cluster galaxies that were previously classified as post-starburst galaxies based on optical spectra. With the help of high-resolution near-infrared (NIR) and optical imaging, Smail et al. (1999) interpreted radio emission from these objects as an indication of ongoing star formation.

Radio surveys of cluster fields have also been useful in the study of cluster evolution. For example, Morrison (1999) found that the population of low-luminosity radio sources in clusters rapidly increases with redshift ($0.02 \leq z \leq 0.41$). This can be interpreted as an extension of the Butcher-Oemler effect (Butcher & Oemler 1984), since the majority of low-luminosity radio sources are found to be blue SF galaxies (Morrison & Owen 2003).

Radio data are key to multiwavelength studies. Radio emission is unobstructed by dust, which avoids a major source of bias found in UV and optical studies. With the addition of far-infrared (FIR) data, radio data can be used to indicate the dominant emission mechanism. The radio luminosity is observationally found to be tightly correlated with the FIR power for SF galaxies locally (Helou et al. 1985; Condon 1992) and at high redshift (Appleton et al. 2004; Ivison et al. 2010; Mao et al. 2011). Any significant departure from the FIR-radio correlation is an indication of AGN activity.

In addition, the positional accuracy of radio surveys can be used to pinpoint counterparts at other wave-

¹ Department of Astronomy, University of Wisconsin-Madison, 475 North Charter Street, Madison, WI 53706, USA; wold@astro.wisc.edu, barger@astro.wisc.edu

² National Radio Astronomy Observatory, P.O. Box O, Socorro, NM 87801, USA; fowen@nrao.edu

³ Academia Sinica Institute of Astronomy and Astrophysics, P.O. Box 23-141, Taipei 10617, Taiwan

⁴ Department of Physics and Astronomy, University of Hawaii, 2505 Correa Road, Honolulu, HI 96822, USA

⁵ Institute for Astronomy, University of Hawaii, 2680 Woodlawn Drive, Honolulu, HI 96822, USA

bands. In the submillimeter, single dish telescopes have very poor resolution, and the unambiguous identification of counterparts is not possible without additional information. From the FIR-radio correlation, we know that FIR luminous SF galaxies, such as submillimeter galaxies (SMGs), are correspondingly luminous in radio emission. Thus, radio data can be used to identify SMG counterparts. Barger et al. (2000), Ivison et al. (2002), and Chapman et al. (2003) found that $\sim 60\%$ of bright (>2 mJy) SMGs had radio counterparts. This feature allowed Chapman et al. (2005) to use radio positions to target spectroscopically a large sample of bright SMGs, establishing the redshift distribution for this population. Bright SMGs are predominantly massive, dust-obscured, SF galaxies at a median redshift of ~ 2.2 (Chapman et al. 2005; Alexander et al. 2005).

Submillimeter observations are a redshift independent probe (due to a negative K -correction: $1 < z < 8$) of dust-reprocessed UV light. However, the positive K -correction of the radio synchrotron emission results in faint observed 1.4 GHz fluxes for high-redshift objects. Thus, a high submillimeter-to-radio flux measurement is an indication of a high-redshift source (Wang et al. 2007, 2009; Dannerbauer et al. 2008; Capak et al. 2008, 2011; Schinnerer et al. 2008; Daddi et al. 2009a,b; Coppin et al. 2009, 2010; Riechers et al. 2010; Knudsen et al. 2010). This extreme population of very massive sources at very high redshifts has been the topic of intense study and has led many authors to suggest the need for significant modifications to models of galaxy evolution (e.g., Granato et al. 2004; Baugh et al. 2005; Hopkins et al. 2005; Lukić et al. 2007). Deep radio surveys continue to be an important tool in the discovery of these objects.

Blank-field submillimeter surveys with the Submillimeter Common-User Bolometer Array (SCUBA; Holland et al. 1999) first resolved the bright SMGs that account for $\sim 20\% - 30\%$ of the $850 \mu\text{m}$ extragalactic background light (e.g., Barger et al. 1998; Hughes et al. 1998; Barger et al. 1999; Eales et al. 1999). These surveys cannot reach the sensitivities required to detect directly the dominant population of < 2 mJy sources because of confusion noise resulting from the coarse resolution of SCUBA. In order to detect this population, one must observe fields with massive cluster lenses to take advantage of both gravitational amplification by the lens and reduced confusion noise (Smail et al. 1997; Cowie et al. 2002; Knudsen et al. 2008). Deep radio images of cluster fields are therefore valuable for identifying the counterparts and determining the properties of this important faint SMG population. Such data will also be very useful for helping to interpret *Herschel* (Egami et al. 2010) and SCUBA2 (C.-C. Chen et al. 2012, in preparation) observations.

In this paper, we construct deep radio catalogs of the cluster fields Abell 370 (A370) and Abell 2390 (A2390), which we have reduced and analyzed in a similar fashion. We derive the number counts for the two fields, and we discuss the influence of the cluster and the importance of cosmic variance on these counts. In our A370 catalog we include redshifts for 200 radio sources that we obtained from the literature, from unpublished work, and from our own observations. We note that, in addition to copious ancillary data, these clusters also have excellent lens models (Kneib et al. 1993; Kneib 2002; Richard et al. 2010). Our radio catalogs in combination with the

TABLE 1
OBSERVING SUMMARY

Field	Config.	Start Date	End Date	On Source Hrs
A370	A	1999 Aug 24	1999 Sep 20	42.4
A370	B	1994 Aug 01	1994 Sep 03	18.4
A2390	A	2008 Oct 20	2008 Oct 28	31.4

public data already available for these extensively studied fields will aid in both cluster and field galaxy studies.

We describe our observations and data reduction in Section 2. In Section 3, we describe our source extraction and cataloging. In Section 4, we compare our catalog to large-area survey results for bright sources. In Section 5, we construct differential number counts for the central regions (radius $< 16'$) of both clusters. We discuss the derived counts in Section 6 and summarize the paper in Section 7. Throughout this paper, our adopted cosmology is $H_0 = 70 \text{ km s}^{-1} \text{ Mpc}^{-1}$, $\Omega_M = 0.3$, $\Omega_\Lambda = 0.7$.

2. OBSERVATIONS AND DATA REDUCTION

2.1. A370 VLA Observations and Data Reduction

We observed the A370 cluster field with the VLA in the A configuration for ~ 42.4 hr on-source during August and September 1999. K. S. Dwarakanath observed A370 in the B configuration for ~ 18.4 hr on-source during August and September 1994. In Table 1, we summarize the parameters of the observing runs. In both configurations, the data were taken in spectral line mode 4, which records seven 3.125 MHz channels in each of the two intermediate frequencies (IFs) centered at 1.365 and 1.435 GHz, and each of the two polarizations. Five and ten second integration times were utilized for the A and B configurations, respectively. Field center is located at $02^{\text{h}}39^{\text{m}}32^{\text{s}}$, $-01^{\circ}35'07''$ in J2000 coordinates. This is offset by approximately 5 arcmins from the cluster center at $02^{\text{h}}39^{\text{m}}50.5^{\text{s}}$, $-01^{\circ}35'08''$.

Since we reduced both the A and B configuration data in a similar fashion, we only describe our reduction of the B configuration data. When necessary, we indicate any significant alterations needed for the A configuration data reduction. Once we completed our initial reduction, we combined the two configuration data sets and performed a final round of calibration. Our data reduction techniques follow the procedures described by Owen & Morrison (2008, hereafter OM08) and Owen et al. (2009). We exclusively used the AIPS package to reduce these data.

We reduced the data obtained during the first day of the observations in the following manner. We edited the phase and flux calibrators for obvious amplitude anomalies using TVFLG. Then, we split the flux calibrator from the raw database and applied a phase self-calibration. At this point, we determined the bandpass correction using the BPASS task applied to the flux calibrator. To account for the effects of the sloping spectral response, we applied this bandpass correction by copying the table generated by BPASS to the raw database. We then scaled the primary flux calibrator, 3C 48, using the Baars flux density values (Baars et al. 1977).

We imaged these data using the AIPS task IMAGR and the three dimensional multifacet options. To image

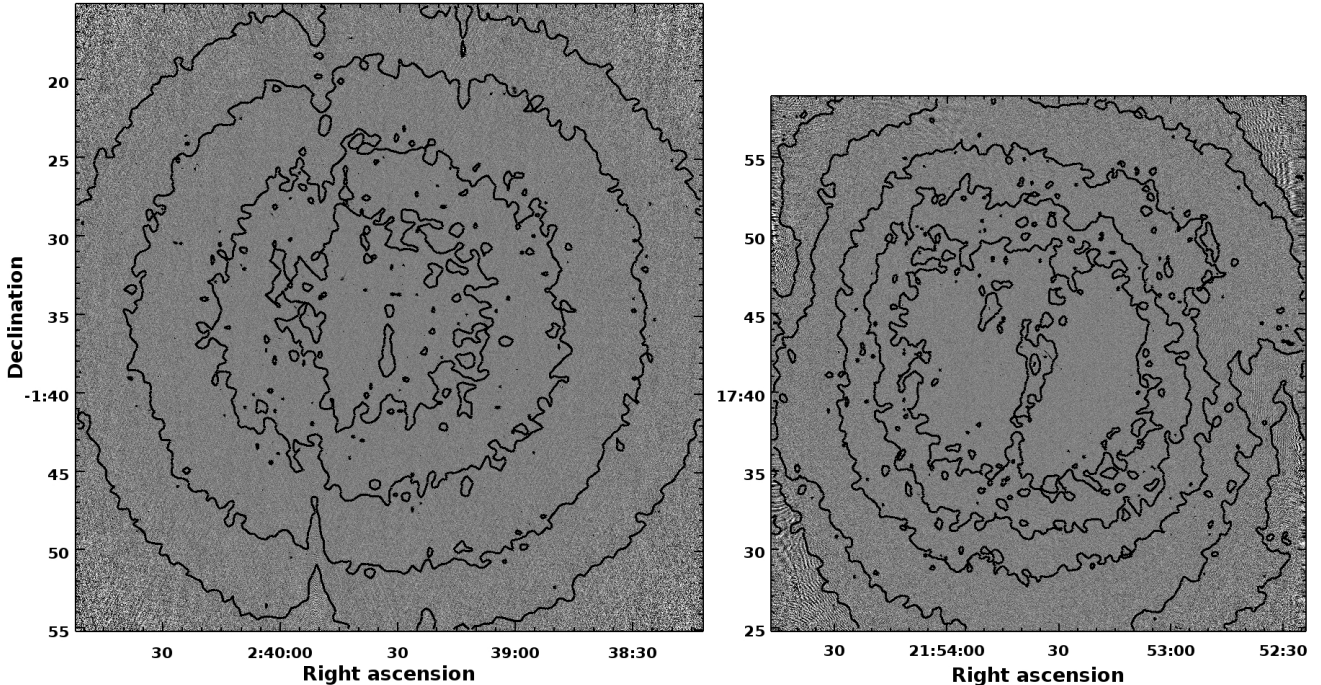


FIG. 1.— *Left*: Contours of constant rms noise overlaid on the $40' \times 40'$ A370 image. Contours levels are 6.5, 8.0, 12.0, and $20.0 \mu\text{Jy}$ and are located approximately 6', 11', 16', and 20' from field center. The image has a 1σ rms noise level of $\sim 5.7 \mu\text{Jy}$ near field center and a $1.8'' \times 1.6''$ synthesized beam. *Right*: Contours of constant rms noise overlaid on the $34' \times 34'$ A2390 image. Contours levels are 5.5, 6.5, 8.0, 12.0, and $20.0 \mu\text{Jy}$ and are located approximately 8', 10', 12', 16', and 19' from field center. The image has a 1σ rms noise level of $\sim 5.6 \mu\text{Jy}$ near field center and a $1.4'' \times 1.3''$ synthesized beam.

0.9° from field center and include all bright NVSS objects within a 2.5° radius required 211 facets, each with 512^2 $1.5''$ pixels. The A configuration required 384 facets (each with 1024^2 $0.5''$ pixels) to image 0.8° from field center and include all strong B configuration sources. After initial imaging, we limited cleaning to real features by designating detected sources with clean boxes. We performed phase self-calibration followed by phase and amplitude self-calibration. Thus, we generated clean images which were then used as fiducial models for each subsequent day.

We employed the VLA pipeline as recommended by AIPS Memo 112 (Lorant Sjouwerman 2007) to perform initial calibration on subsequent days. Then, we calibrated these data to images produced from the day one observations. We used the AIPS procedure STUFFER to combine and compress data from all days of the observing run, producing one master visibility file (for each configuration).

We then split this combined visibility data set by IF and further self-calibrated. As discussed in Owen et al. (2009), we used UVSUB to subtract the bright off-axis sources from the visibility data. We then imaged the facets known to contain bright, outlying sources as a data cube. We subtracted the generated clean components from the original visibility data channel by channel. We conducted this residual spectral subtraction procedure to compensate for frequency-dependent artifacts which produce radial smearing for very bright sources far from field center.

We then combined the like components of the A and B array with DBCON and further split the data into 2 polarizations, thus producing 4 visibility files (2 polarizations and 2 IFs). We further calibrated these data,

including another iteration of the residual spectral subtraction procedure. As a final calibration step, we employed PEELR to account for local gain variations produced by bright sources in the outskirts of the field. Final images were made using robust weighting (ROBUST=0 in IMAGR) and using IMAGR's UVTAPER empirically set to 100,100. We combined the facet images into 4 composite images using FLATN. Then, we combined these 4 images, weighted by rms^{-2} . Finally, we flattened the image composite using MWF (as performed in OM08, but with a 41×41 pixel support window). This final image has a noise level of $\sim 5.7 \mu\text{Jy}$ rms near field center, with a $1.8'' \times 1.6''$ synthesized beam at a position angle of 166° . In Figure 1(a), we show the 40×40 arcmin² A370 radio field with rms noise contours overlaid. Residual sidelobes from bright outlying sources are still clearly present on either side of the field center, offset by approximately 6' from center with a North-South orientation. In Figure 2, we show a larger image of the A370 radio field without noise contours to allow for inspection of individual radio sources. We observe no radio halos or relics; however, smaller array configurations would be more sensitive to these large structures.

2.2. A2390 VLA Observations and Data Reduction

We observed the A2390 cluster field with the VLA in the A configuration for ~ 31.4 hr on-source during October 2008. We obtained the data in spectral line mode 4, and we sampled the data every 3.3 seconds. Field center is located at $21^{\text{h}}53^{\text{m}}36^{\text{s}}$, $+17^\circ 41' 52''$ in J2000 coordinates.

As described above for the A370 field, we followed the data reduction techniques outlined by OM08 and Owen et al. (2009). The primary flux calibrator was 3C 48.

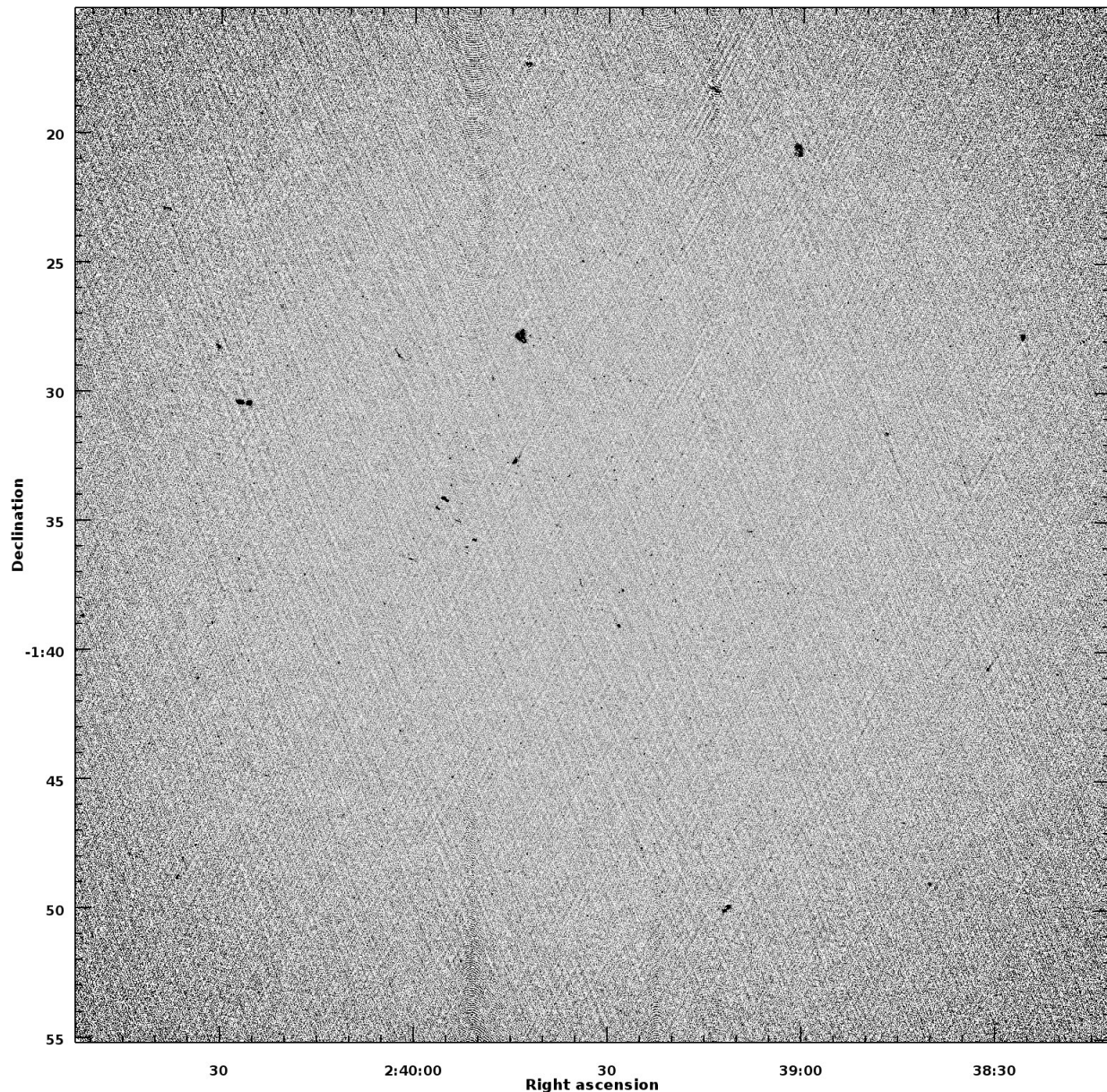


FIG. 2.— The $40' \times 40'$ A370 image. Field center is located at $02^h 39^m 32^s$, $-01^\circ 35' 07''$ in J2000 coordinates. This is offset by $\sim 5'$ from the cluster center at $02^h 39^m 50.5^s$, $-01^\circ 35' 08''$. We observe no radio halos or relics; however, smaller array configurations would be more sensitive to these large structures.

We used 102 facets to cover the primary beam. Each facet consisted of 1024^2 $0.5''$ pixels. We carried out the reductions as described above, producing a master visibility file for all A configuration data. After an initial pass of self calibration, we split the visibility file into the 28 parts that come from the 7 channels, 2 IFs, and 2 polarizations. We self-calibrated, imaged, cleaned, and PEELRed the 28 data sets independently. We carried out a few self-calibration/imaging/PEELR cycles to obtain a converging solution for each of the 28 data sets. We then made 28 images with the AIPS task IMAGR. This procedure, which further splits the visibility files by channel, was necessary to minimize the sidelobes from the bright sources around the edges of the field and from the central cD galaxy.

We combined the 28 images using IDL. For each pixel in the 28 images, we first measured the local background

fluctuation in a $32'' \times 32''$ region around it. Such background fluctuations come from both noise and weak residual sidelobes from bright sources that cannot be perfectly calibrated with the above procedure. We then merged the 28 images using an error-weighted mean according to the above measured background fluctuation. Very weak residual sidelobes can still be seen in the final merged image in certain regions, especially along the North-South side of the central cD galaxy. However, we obtained an excellent overall $5.6 \mu\text{Jy}$ rms in the central part of the image. The synthesized beam is $1.4'' \times 1.3''$ with a position angle of 72° . In Figure 1(b), we show the $34 \times 34 \text{ arcmin}^2$ A2390 radio field with rms noise contours overlaid. In Figure 3, we show a larger image of the A2390 radio field without noise contours to allow for inspection of individual radio sources. We observe no radio halos or relics; however, smaller array configurations

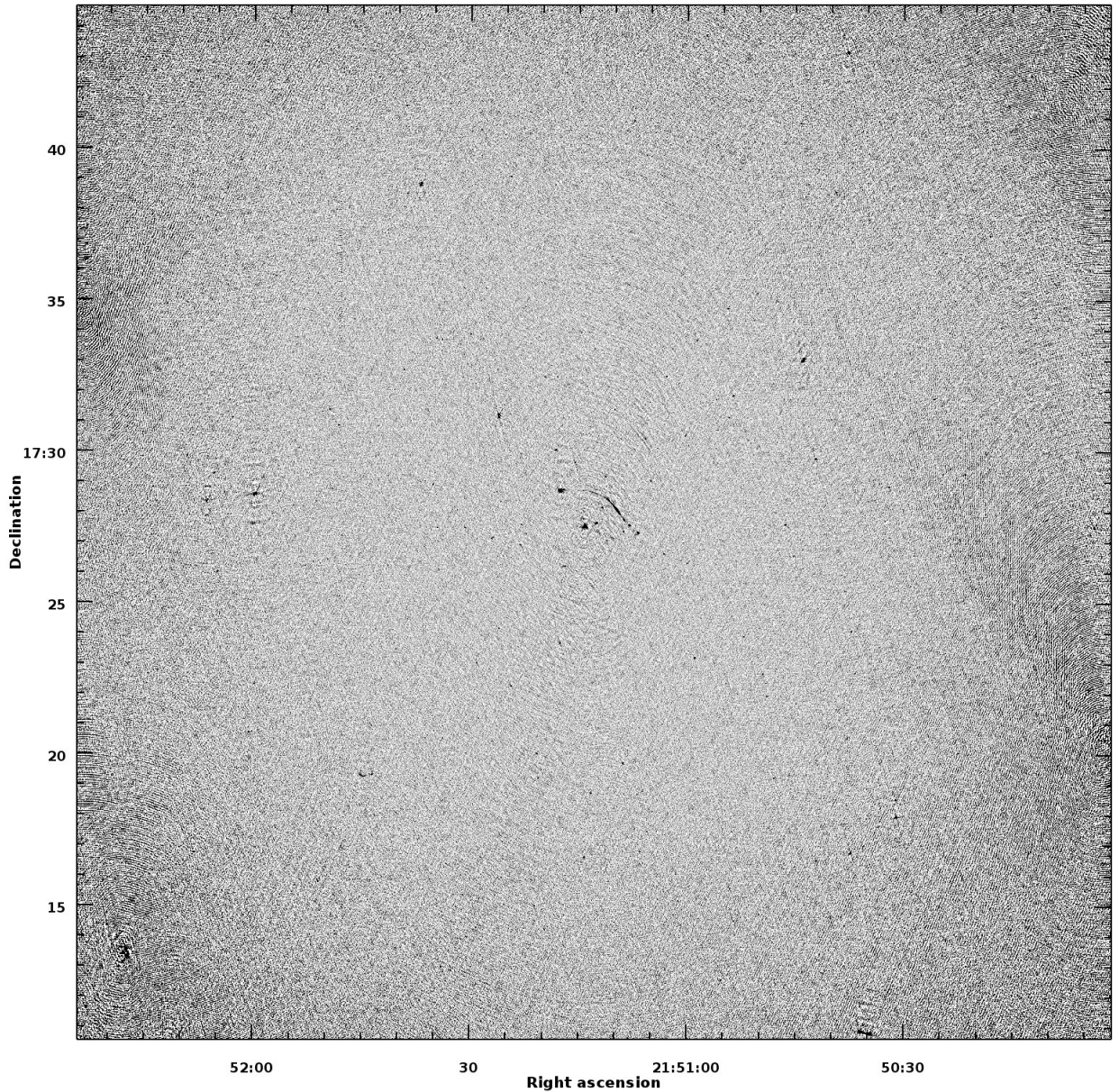


FIG. 3.— The $34' \times 34'$ A2390 image. Field center is located at $21^{\text{h}}53^{\text{m}}36^{\text{s}}$, $+17^{\circ}41'52''$ in J2000 coordinates. This is only offset by $20''$ from the cluster’s central cD galaxy at $21^{\text{h}}53^{\text{m}}37^{\text{s}}$, $+17^{\circ}41'44''$. We observe no radio halos or relics; however, smaller array configurations would be more sensitive to these large structures.

would be more sensitive to these large structures.

2.3. A370 Spectroscopic Observations and Reductions

We targeted 58 radio sources without existing spectral data using the Hydra fiber spectrograph on the Wisconsin-Indiana-Yale-NOAO (WIYN) telescope. We preferentially targeted optically bright galaxies. We observed these data with a single two hour pointing on 2012 January 20. Seeing was approximately $0.8''$. We configured the spectrograph using the “red” fiber bundle and the 316@7.0 grating at first order with the GG-420 filter to provide a spectral window of $\sim 4500 - 9500 \text{ \AA}$ with a pixel scale of 2.6 \AA per pixel. The Hydra “red” fibers are $2''$ in diameter and have a positional accuracy of $0.3''$, which ensured that the majority of light from our target galaxies was observed with little contamination from the sky and neighboring sources. We employed

the IRAF task *dohydra*⁶ in the reduction of our spectra. This task is specifically designed for reduction of data from the Hydra spectrograph and includes steps for dark and bias subtraction, flatfielding, dispersion calibration, and sky subtraction. As described in Keenan et al. (2012), we used the IRAF task *xcsao* within the *rvsao* package (Kurtz & Mink 1998) to determine redshifts for our observed spectra. Of the 58 targets, we obtained high-confidence redshifts for 36.

3. SOURCE EXTRACTION AND CATALOGING

For the A370 image, we extracted sources from the central $40 \times 40 \text{ arcmin}^2$ region. For the A2390 image, we extracted sources from the central $34 \times 34 \text{ arcmin}^2$ region. To help account for instrumental and intrinsic im-

⁶ <http://iraf.noao.edu/tutorials/dohydra/dohydra.html>

TABLE 2
SAMPLE OF RADIO SOURCE CATALOG

Abell Field (1)	Number (2)	R.A. (J2000) hms \pm e(s) (3)	Dec. d ' ' \pm e('') (4)	PNR (5)	S _{1.4} \pm e μ Jy (6)	Maj (7)	Size Min (8)	P.A. (9)	Upper '' (10)	Beam '' (11)	Redshift (12)	Ref. (13)
370	0	02 38 13.15 0.439	-01 46 26.57 0.55	25.4	1422.9 \pm 74.3	5.8	3.9	59	...	1.8
370	1	02 38 13.83 0.095	-01 17 30.36 0.12	5.3	705.1 \pm 134.5	0.5	3.0
370	2	02 38 14.64 0.070	-01 34 15.05 0.06	23.5	610.7 \pm 31.8	1.6	1.8
370	3	02 38 15.07 0.192	-01 51 24.19 0.22	7.9	575.6 \pm 75.1	3.2	3.0
370	4	02 38 15.50 0.110	-01 55 2.76 0.10	5.3	1005.1 \pm 190.3	1.8	1.8
370	5	02 38 16.61 0.292	-01 33 0.89 0.21	13.0	207.8 \pm 25.6	7.2	0.0	60	...	1.8
370	6	02 38 16.62 0.400	-01 27 58.24 0.53	934.8	31519.4 \pm 946.3	6.7	3.8	103	...	1.8
370	7	02 38 16.89 0.416	-01 53 6.26 0.54	39.4	4367.0 \pm 177.2	6.7	3.9	42	...	1.8
370	8	02 38 17.26 0.421	-01 50 41.28 0.54	32.2	3195.5 \pm 145.4	6.0	3.2	48	...	1.8
370	9	02 38 17.35 0.221	-01 52 46.70 0.37	5.3	390.1 \pm 73.9	4.2	1.8

NOTE. — Table 2 is published in its entirety in the electronic edition of *Astrophysical Journal Supplement*. A portion is shown here for guidance regarding its form and content.

age broadening effects, we also analyzed our images at lower resolutions. For each field, we created two complementary low resolution images by convolving the final images with Gaussians with FWHM equal to 3'' and 6''. We extracted sources from the full, 3'', and 6'' resolution images independently. We then compared and collated the results. This procedure has been shown to assist in the detection of low surface brightness sources (Morrison et al. 2010).

We generated noise maps using the AIPS routine RMSD (IMSIZE=71,-1; OPTYPE='HIST') for each of the three resolutions. When extracting sources using the AIPS routine SAD, we used the output of RMSD to estimate the background noise. SAD searches an image for sources above some peak flux threshold and then uses a Gaussian fitting routine to estimate flux density. For each resolution, we extracted sources with peak signal-to-noise ratios (PNRs) greater than 4. For sources with $\text{PNR} \leq 5.5$ or for residual sources found manually, we used JMFIT to determine source properties. The final catalog contains sources with PNRs greater than 5. We accounted for bandwidth smearing and primary beam attenuation in both the SAD and JMFIT procedures.

We considered a source resolved if the lower limit for the major axis is greater than zero and the integrated flux minus 1σ error exceeds the peak flux. For unresolved sources, we recorded the upper limit of the major axis and the total flux (best estimated by the peak flux, OM08). For resolved sources, we recorded the integrated flux and the best fit deconvolved major, minor, and position angle (P.A.).

For extended sources, it is more accurate to estimate the flux densities using TVSTAT, which sums the total signal in a user-defined area, rather than using the summation of the SAD Gaussians. As prescribed by Morrison et al. (2010), we used IMEAN to determine the peak flux and its location. Using the noise map, we then measured the 1σ noise level at this position. We adopted the ratio of these values, peak flux / 1σ noise level, as the PNRs for extended sources.

For each field, we compared the three catalogs extracted from the three images with different resolutions. We adopted the 3'' resolution source only if the PNR was more than 10% higher than its higher resolution counterpart. Similarly, we adopted the 6'' resolution source only

if the PNR was more than 10% higher than its 3'' resolution counterpart. Thus, we generated a catalog for the A370 and A2390 fields.

We compared an intermediate image constructed just after combination of the A and B configurations to our final A370 image. We found that the extracted source flux is underestimated by a factor of 1.1. We attribute this discrepancy to calibration errors from combining the A and B configuration data. In our data reduction routine, we performed self calibration of the combined data without constraining the mean gain modulus to unity. In the presented A370 catalog, we have corrected for this systematic offset.

We present the first ten lines of our combined A370 and A2390 catalog in Table 2. In Column 1, we indicate the Abell field, either Abell 370 or 2390. In Column 2, we indicate the radio source number. There are a total of 699 galaxies in the A370 catalog and 524 galaxies in the A2390 catalog. In Columns 3 and 4, we give the (J2000) right ascension and declination with error estimates. We report the peak signal-to-noise ratio in Column 5. In Column 6, we indicate the total 1.4 GHz flux and uncertainty in μ Jy. For resolved sources, we list the best-fit deconvolved size characteristics in Columns 7–9, reporting the major and minor FWHM sizes in arcsec. For unresolved sources, we indicate the major axis upper limit size in Column 10. We list the resolution of the image used in the source extraction in Column 11.

Only the A370 field contains data in Columns 11 and 12. In these columns, we list 200 A370 redshifts and their references. To identify redshift - radio matches, we visually inspected all spectroscopic data lying within 10'' of a radio source position by overlaying radio contours and the spectral position on deep broadband optical images. We adopted this technique, because extended and double-lobe radio sources often have peak radio brightness offset from their optical center. Although these redshifts have been utilized in previous studies, the vast majority are published for the first time. Reference 1 designates redshifts obtained via an ongoing spectroscopic campaign using the DEep Imaging Multi-object Spectrograph (DEIMOS) on the Keck telescope (L. Cowie, private communication). Reference 2 denotes a campaign by F. Owen using Hydra on WIYN (F. Owen, private communication). Reference 3 designates addi-

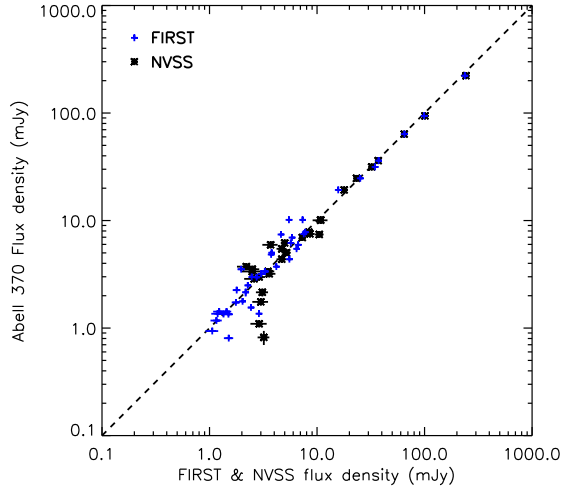


FIG. 4.— A370 flux densities compared to those from the FIRST and NVSS catalog. 41 out of 50 FIRST objects (blue crosses) and 29 out of 30 NVSS objects (black asterisks) are found to have counterparts. The dashed line indicates the ideal case, equality of flux densities. (A color version of this figure is available in the online journal.)

tional WIYN Hydra redshifts obtained in a $z \sim 0.2$ NIR follow-up survey (Keenan et al. 2012). Reference 4 denotes an archival redshift obtained from Dunlop et al. (1989). Reference 5 designates the new WIYN Hydra redshifts that we obtained (see Section 2.3) to supplement the existing data. We determine the redshift false identification rate by shifting the radio image by $70''$ and re-identifying redshift - radio matches. We estimate that 4% of our redshift identifications are false.

4. COMPARISON WITH NVSS AND FIRST

We compare our work to the Faint Image of the Radio Sky at Twenty-cm (FIRST) (White et al. 1997) and the NRAO VLA Sky Survey (NVSS) (Condon et al. 1998) catalogs. The FIRST survey is a VLA program which produced images with 0.75 mJy sensitivity and a resolution of $\sim 5''$ in the vicinity of A370. This survey has 50 sources coincident with our 40×40 arcmin² A370 field. Of these 50 objects, 41 have counterparts in our catalog. NVSS provides ~ 2.5 mJy sensitivity and a resolution of $45''$. There are 30 NVSS sources in our A370 field. Twenty-nine of these have counterparts in our radio catalog.

Based on all 41 FIRST sources with counterparts in our radio catalog, the mean $(S_{1.4 \text{ GHz}}^{\text{FIRST}}/S_{1.4 \text{ GHz}}^{\text{A370}}) = 1.01 \pm 0.05$. Based on the 25 sources brighter than the ~ 2.5 mJy NVSS sensitivity limit that also have counterparts, the mean $(S_{1.4 \text{ GHz}}^{\text{NVSS}}/S_{1.4 \text{ GHz}}^{\text{A370}}) = 0.98 \pm 0.04$. Figure 4 compares our flux density measurements with those of NVSS and FIRST. We find no systematic offset between our flux densities and the FIRST and NVSS flux densities.

The FIRST survey does not cover the A2390 cluster field. The NVSS catalog contains 18 objects within our A2390 field. Seventeen of these objects have counterparts in our catalog. Based on the 16 sources brighter than the ~ 2.5 mJy NVSS sensitivity limit that also have counterparts, the mean $(S_{1.4 \text{ GHz}}^{\text{NVSS}}/S_{1.4 \text{ GHz}}^{\text{A2390}}) = 1.05 \pm 0.12$. Figure 5 compares our flux density measurements with those of NVSS. We find no systematic offset between our flux densities and the NVSS flux densities.

We believe that most, if not all, non-overlapping NVSS

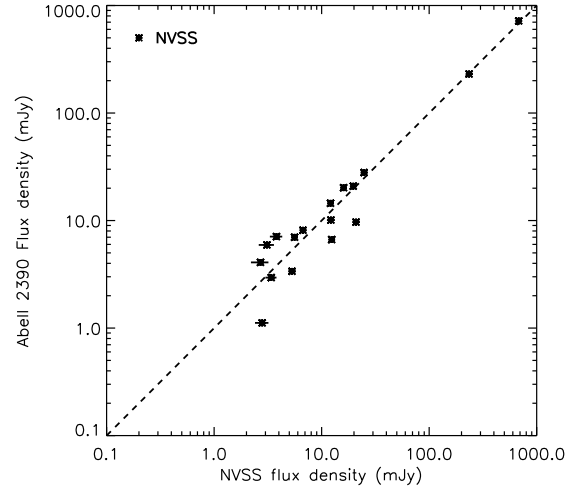


FIG. 5.— A2390 flux densities compared to those from the NVSS catalog. Of the 18 NVSS objects in our survey area, 17 (black asterisks) are found to have counterparts. The dashed line indicates the ideal case, equality of flux densities.

and FIRST sources are false detections. Inspection of our images reveals no viable counterparts. The two NVSS sources without counterparts have cataloged flux densities of 2.7 mJy (A370 field) and 2.8 mJy (A2390 field), which are very close to the NVSS sensitivity limit. The non-overlapping object in the A370 field also has no FIRST counterpart. The NVSS catalog only gives upper limits for the major and minor deconvolved sizes, indicating that these objects should be relatively compact. The nine non-overlapping FIRST objects may be judged based on their reported sidelobe probability values, which give the likelihood that a source is spurious. Spurious sources are commonly due to artifacts created by nearby bright sources (White 2008). We find that there is a 60% mean probability that these 9 sources are spurious. Approximately 95% of FIRST sources have sidelobe probabilities that are lower than this mean value.

5. SOURCE COUNTS

We constructed the differential source counts for the central region (radius $< 16'$) of each fields. These areas allow for the 5σ detection of all point sources above $\sim 60 \mu\text{Jy}$ (see Figure 1). The A370 and A2390 catalogs contain 529 and 380 objects, respectively, with $37 < S_{1.4 \text{ GHz}} < 3000 \mu\text{Jy}$ that lie within the areas of interest. In the first three columns of Tables 3 and 4, we list the the 1.4 GHz flux bins, the flux bin centers in log space, and the number of sources found per bin.

We assess the significance of false detections (5σ noise spikes) by performing an identical source extraction procedure on the inverted radio image (see Ibar et al. 2009 for a similar procedure). We generate the inverted image by multiplying all pixel values by -1. This analysis assumes that positive noise spikes are as likely as negative noise spikes. Overall, we find that $\sim 8\%$ of our cataloged sources are likely to be false detections (see Column 4 of Tables 3 and 4 for the number of false sources found per flux bin). We subtract the false detections per bin from our raw counts. We show the small effect of this correction on our final results in Figure 11.

To determine the completeness of our catalog, we de-

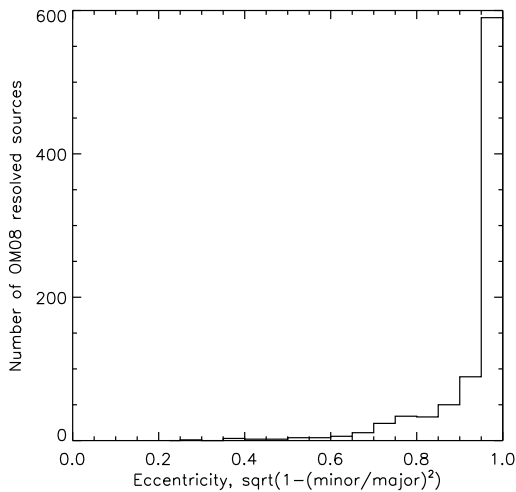


FIG. 6.— Eccentricity distribution of resolved OM08 radio sources. The high level of observed eccentricity is the motivation behind our one-dimensional simulated sources. These sources modified by instrumental effects are used to assess the completeness of our catalog.

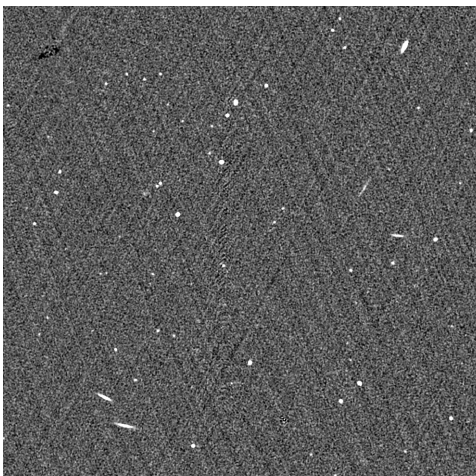


FIG. 7.— $8' \times 8'$ cutout of a simulated image. The recovery rate of the simulated sources determines the correction factors applied to our number counts. The background template is a residual, source extracted, SAD image of the cluster field. SAD poorly extracts extended sources, leaving a non-representative background. We prevent simulated sources from populating these regions. The area affected is less than 1% of the total field area. We show a region with a poorly extracted extended source in the upper left corner. See Section 5 for details.

veloped a simple Monte Carlo simulation that accounts for major instrumental and extraction inefficiencies. For the background template, we used a residual, source extracted, SAD image (see Biggs & Ivison 2006 for a similar setup). We removed all detections above 4.5σ from this background image. We randomly positioned one thousand sources within the area of interest, a $16'$ radius circle. However, we prevented sources from populating areas with poorly extracted extended sources. This affected less than 1% of the total area. We randomly sampled the object's flux from a Euclidean power law distribution with a minimum flux threshold of 4.5σ . We randomly selected the object's major axis from the OM08 distribution, shown in their Figure 8 and assign a random position angle. Based on the observed eccentricity of faint radio sources (e.g. see our Figure 6 for

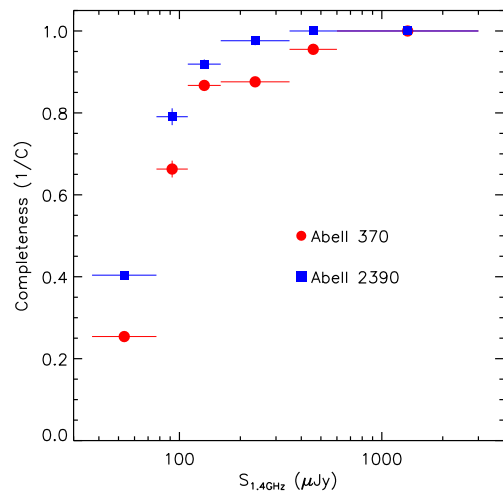


FIG. 8.— Monte Carlo simulation results. The completeness, or number of recovered sources per number of input sources, as a function of flux density. (A color version of this figure is available in the online journal.)

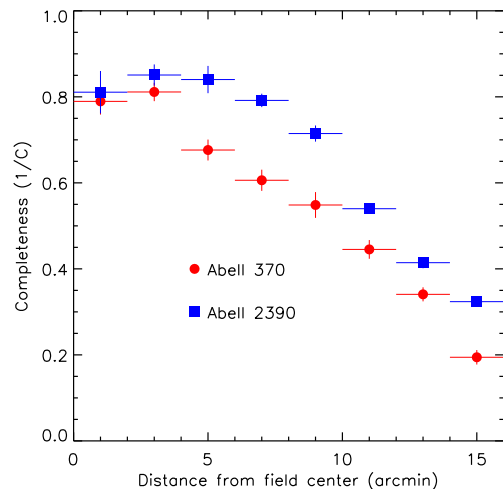


FIG. 9.— Monte Carlo simulation results. The completeness, or number of recovered sources per number of input sources, as a function of radius from field center. (A color version of this figure is available in the online journal.)

the OM08 eccentricity distribution), we assumed an unresolved minor axis. All sources initially had a Gaussian flux profile. We convolved the object with the beam and then radially convolved the object with a Gaussian, with $\text{FWHM} = (\text{distance from field center}) \times (\text{channel bandwidth}) / (\text{central frequency})$. The later convolution accounted for bandwidth smearing. Finally, we modified the gain to account for primary beam attenuation. The simulation did not account for finite time-average smearing, which we estimate would broaden sources by a few percent. We show an $8' \times 8'$ cutout of a simulated image in Figure 7.

We perform the extraction technique described in Section 3 on the simulated image. We complete this procedure 5 times, providing a total of 5000 simulated sources per field. The recovery rate between the known input and the extracted output gives the correction factors, C , listed in Column 5 of Tables 3 and 4 and displayed in Figures 8 and 9. In Figure 10, we show how the variation of the 5 Monte Carlo simulations affects our derived

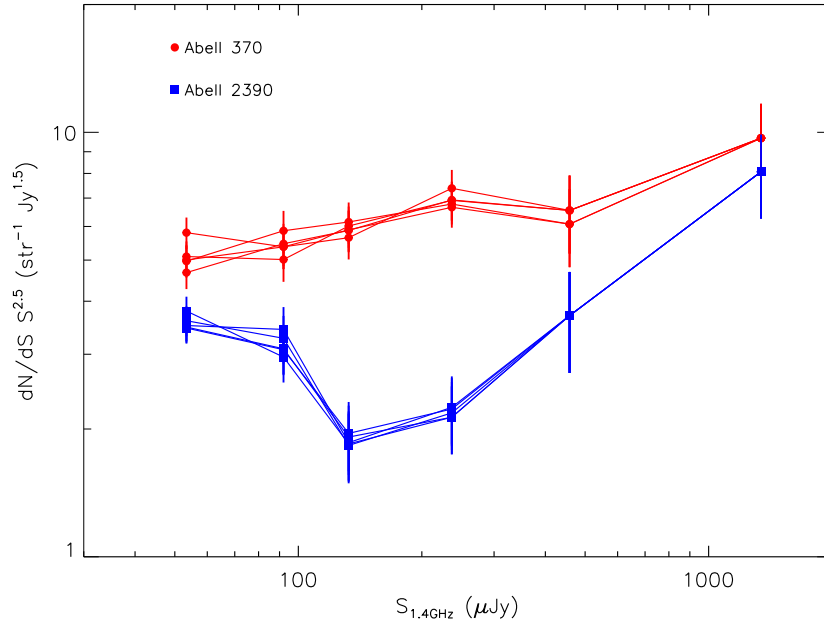


FIG. 10.— Five Monte Carlo completeness results per field applied to our A370 and A2390 counts. We use the variation of the Monte Carlo results to estimate the error in the derived correction factors. This error is less than or approximately equivalent to the Poisson error (displayed error bars). (A color version of this figure is available in the online journal.)

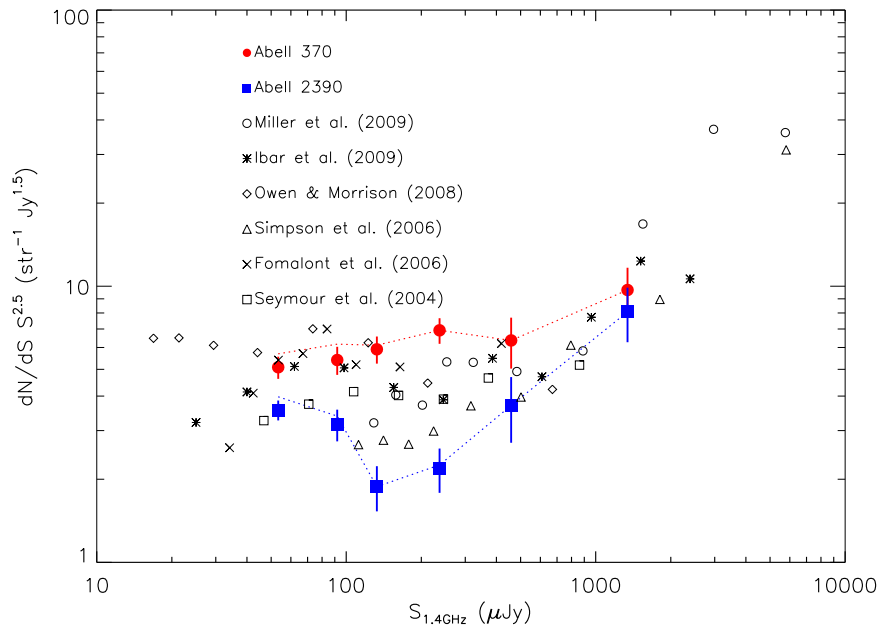


FIG. 11.— A370 and A2390 differential source counts compared to blank field counts and Coma cluster counts (Miller et al. 2009). The dotted lines indicate the effect on our derived counts of not correcting for false detections. (A color version of this figure is available in the online journal.)

counts. We calculate the corrected counts using the following equation:

$$N_{corr} = (N - N_{false}) \times C.$$

We then divide N_{corr} by the survey area and the bin width. We normalize these values by the Euclidean slope $S^{-2.5}$, where S is bin center in log space. We summarize the final results in Column 6 of Tables 3 and 4. In Figure 11, we show the A370 (red circles) and A2390 (blue squares) number counts with error bars indicative

of Poisson uncertainty and Monte Carlo variation. We use dotted lines to indicate the effect on our derived counts of not correcting for false detections. We use open black circles to show number counts constructed from a VLA Coma cluster survey (Miller et al. 2009). We also show various blank field counts (black: asterisks, diamonds, triangles, crosses, and squares) for comparison to our A370 and A2390 number counts.

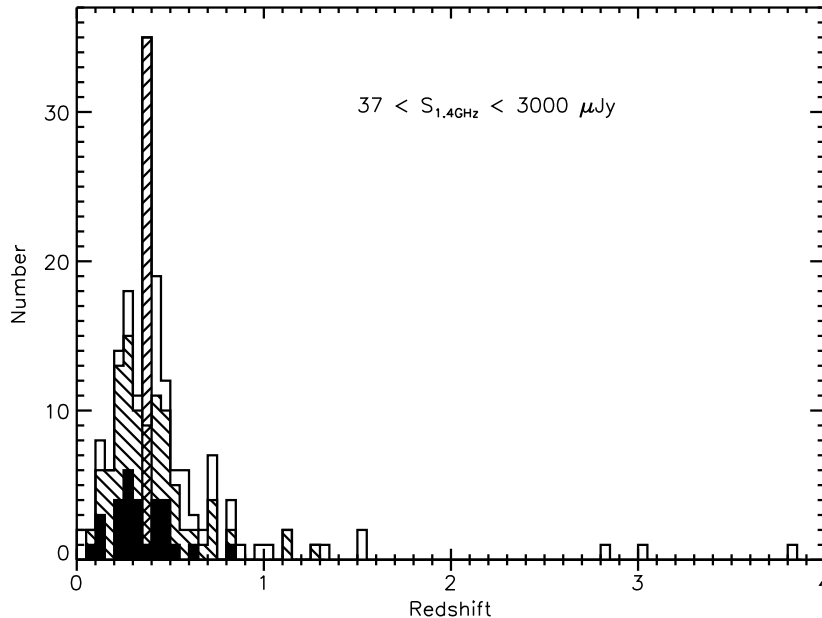


FIG. 12.— A histogram of the 167 redshifts in our A370 number counts sample. The outer outline of the histogram indicates the redshift distribution of the entire 167 objects. The three interior filled histograms display the effect of applying cluster masks. The histogram filled with positive-slope diagonal lines designates the 35 cluster members that were excluded in our $z_{A370} \pm 0.025$ mask. The histogram filled with negative-slope diagonal lines designates the spectroscopically identified sources that lie beyond a $6'$ radius from the cluster center. Our $6'$ radius cluster mask excludes 26 (74%) of the spectroscopically identified cluster members. The filled histogram designates the spectroscopically identified sources that lie beyond $12'$ radius from the cluster center. Our $12'$ radius cluster mask excludes 34 (97%) of the spectroscopically identified cluster members.

TABLE 3
A370 1.4 GHz RADIO SOURCE COUNTS.

S bin (μJy)	S (μJy)	N	N_{false}	C	$S^{2.5}dN/dS$ ($\text{Jy}^{1.5}\text{sr}^{-1}$)
37 - 77	53	189	20	3.9	5.1 ± 0.5
77 - 110	92	113	14	1.5	5.4 ± 0.6
110 - 160	133	89	3	1.2	5.9 ± 0.7
160 - 350	237	91	0	1.1	6.9 ± 0.7
350 - 600	458	23	0	1.0	6.4 ± 1.3
600 - 3000	1342	24	0	1.0	9.7 ± 2.0

TABLE 4
A2390 1.4 GHz RADIO SOURCE COUNTS.

S bin (μJy)	S (μJy)	N	N_{false}	C	$S^{2.5}dN/dS$ ($\text{Jy}^{1.5}\text{sr}^{-1}$)
37 - 77	53	210	22	2.5	3.6 ± 0.3
77 - 110	92	74	5	1.3	3.2 ± 0.4
110 - 160	133	29	0	1.1	1.9 ± 0.3
160 - 350	237	33	1	1.0	2.2 ± 0.4
350 - 600	458	14	0	1.0	3.7 ± 1.0
600 - 3000	1342	20	0	1.0	8.1 ± 1.8

The A370 number counts form an upper envelope to the blank field number counts. This could potentially be explained by an over-density of cluster galaxies superimposed on the $z \sim 1$ field galaxies. In addition to the galaxy cluster at $z = 0.375$, Keenan et al. (2012) found galaxy over-densities at $z \sim 0.18$ and $z \sim 0.25$. We clearly see evidence for the $z \sim 0.25$ over-density in the redshift distribution (see Figure 12).

The A2390 number counts form a lower envelope to the blank field number counts, which is more surprising.

This might indicate that the galaxy cluster at $z=0.228$ does not significantly contribute to a sparsely populated field of $37 < S_{1.4\text{GHz}} < 3000 \mu\text{Jy}$ galaxies.

In the following, we investigate disentangling the cluster galaxy population from the field galaxy population using two techniques. 1) *Redshift mask*: For the A370 field, we re-derive the number counts with all the spectroscopically confirmed cluster members excluded. We lack sufficient spectroscopic data to perform a similar analysis on A2390. 2) *Radial masks*: We re-derive the number counts for both fields with the cluster center masked. In other words, we re-derive the number counts within a range of annuli to eliminate the majority of cluster objects. As we reduce the influence of the cluster, we note the effect that has on the number counts.

6.1. Redshift Mask

Our large sample of A370 redshifts allows us to re-derive the number counts after excluding known cluster members. To construct the A370 number counts, we used the 529 sources with $37 < S_{1.4\text{GHz}} < 3000 \mu\text{Jy}$ that lie within $16'$ of the field center. Of these, 167 (32%) have known redshifts. In Figure 12, we show the distribution of these redshifts. We define cluster members as any object with $z_{A370} \pm 0.025$. Rather than a physical cluster scale, we base the redshift range on a conservative estimate of the redshift error. Using this criteria, we identify 35 objects as cluster members, and we exclude them from the re-derived counts. In Figure 12, we use positive-slope diagonal lines to denote the cluster members. We note that our spectroscopic completeness declines as the 1.4 GHz flux decreases and as the projected distance from the cluster center increases. Given these biases and the proximity of the cluster members compared to the average field galaxy at $\langle z \rangle \sim 1$, we expect to have succeeded

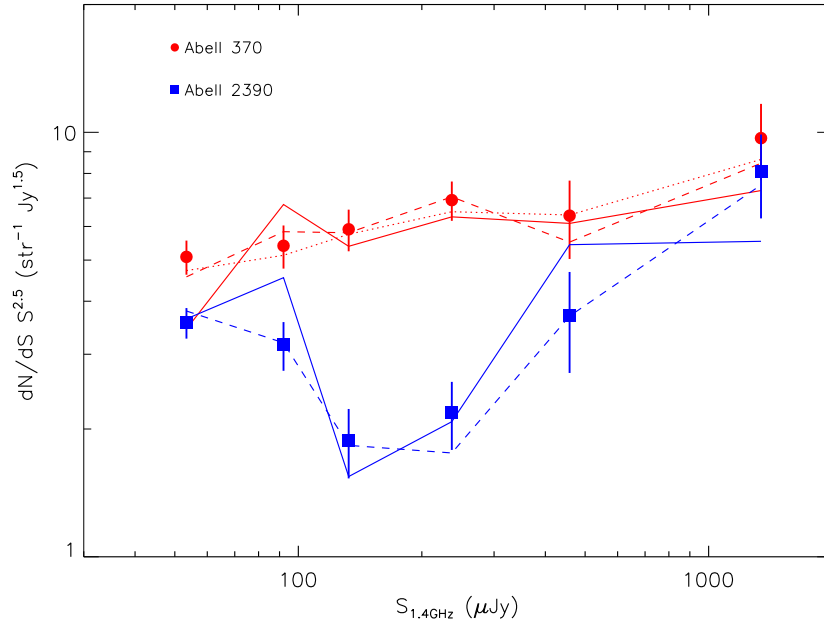


FIG. 13.— Illustration of the effect on our derived number counts of applying radial cluster masks. Symbols with error bars indicate the cluster counts with no mask applied (full 16' radius field). The dashed lines indicate the counts with a radial area of 6' from the cluster centers masked. The solid lines indicate the counts with a radial area of 12' from the cluster centers masked. The red dotted line indicates the counts with spectroscopically confirmed A370 cluster members excluded. On average, the A370 counts are reduced, bringing them in closer agreement to blank field results. The A2390 counts are consistently low. Even taking into account the greater Poisson error of the more restrictive masks, the counts in the two cluster fields are found to be inconsistent with one another in the 110 - 350 μJy flux range. (A color version of this figure is available in the online journal.)

in excluding more than 32% of the cluster members.

We show the re-derived number counts in Figure 13 as a red dotted line. We find that the A370 counts are lowered by a weighted average of $5.7\% \pm 6.5\%$. The estimated error in our weighted average calculation (6.5%) results from propagating the Poisson error of our measured counts. Although not corrected for, excluding spectroscopic cluster members will also remove the cluster's effective volume. This will reduce the survey's effective area and therefore increase the re-derived counts. This effect is small (estimated to be on the order of a few percent), since the effective volume of our radio field is large when compared to the effective volume of the cluster. Given our spectroscopic completeness of 32%, we expect the systematic uncertainty in our estimate of cluster influence to be dominated by any unidentified cluster members. Thus, we regard the reported $5.7\% \pm 6.5\%$ reduction in our re-derived counts as a lower limit.

6.2. Radial Masks

We also re-derive the number counts with cluster center radial masks. We apply masks to eliminate all galaxies within 2', 4', 6', 8', 10', and 12' from the cluster center. We obtain an estimate of the effectiveness of removing cluster members from both fields using radial masks by considering the cluster evolution study of Morrison (1999, hereafter M99). M99 investigated the radial distribution of low-luminosity ($10^{22.3} < L_{1.4\text{GHz}} < 10^{23}$ W Hz^{-1}) radio galaxies (LLRGs) for a $z < 0.25$ and a $z \sim 0.4$ cluster sample. The low-redshift sample was composed of 76 cluster LLRGs, while the $z \sim 0.4$ sample was composed of 43 cluster LLRGs.

From M99's derived cumulative radial density profile (his Figure 6.18), we see that a 1.9 Mpc (6' radius) A370

mask should exclude $\sim 82\%$ of the cluster's LLRG population, while a 3.7 Mpc (12' radius) mask should exclude $> 97\%$. The 1.3 Mpc (6') and 2.6 Mpc (12') A2390 masks should exclude $\sim 82\%$ and $\sim 97\%$ of the cluster's LLRGs, respectively. LLRGs correspond to galaxies with flux densities between 41 - 206 μJy for the A370 cluster and 129 - 648 μJy for the A2390 cluster. The radial distributions of higher luminosity radio sources are found to be more centrally compact. Thus, we expect our masks to reduce significantly the population of all $S_{1.4\text{GHz}} > 129$ μJy (> 41 μJy for A370) cluster sources. There are uncertainties in this estimate, since individual clusters will have deviations from this averaged radial profile. Additionally, the M99 study notes a lack of confirmed outer cluster members in the $z \sim 0.4$ sample, which may bias this radial profile. As a check on these percentages, we note how many spectroscopically confirmed cluster members remain after applying the A370 radial masks. Figure 12 shows the redshift histogram before and after the application of the 6' (histogram filled with negative-slope diagonal lines) and the 12' (filled histogram) masks. Our 6' and 12' cluster masks remove 74% and 97% of the spectroscopically identified cluster members, respectively. This estimate, while roughly consistent with the M99 result, suffers from our spectroscopic incompleteness, which gets worse with increasing radius and decreasing flux. We conclude that our 6' radial masks should significantly reduce cluster influence on the derived number counts. We adopt the 12' mask result as our best estimate of the total cluster influence.

In Figure 13, we show the number counts after excluding radial areas of 6' (*dashed*) and 12' (*solid*) from the cluster centers. These angular radii, respectively, correspond to 1.9 and 3.7 Mpc at $z_{\text{A370}} = 0.375$ and 1.3 and 2.6 Mpc at $z_{\text{A2390}} = 0.228$. The A370 field has a 5.0 Mpc

(16') radial extent, while the A2390 field has a 3.5 Mpc (16') radial extent. Excluding radial areas of 6' and 12' from the A370 cluster center reduces the number counts by a weighted average of $3.5\% \pm 7.4\%$ and $7.6\% \pm 10.7\%$. If we also exclude any additional spectroscopically identified cluster members not in the masked regions, then these percentages increase by 1%. Excluding radial areas of 6' and 12' from the A2390 cluster center reduces the number counts by an average of $0.7\% \pm 8.8\%$ and $1.1\% \pm 15.1\%$. In Figure 13, we can see that the re-derived number counts in A2390 are consistently low in the 110 to 350 μJy range, even when compared to the lowest blank field results.

Our best estimate indicates that the A370 cluster influences the derived number counts on the 10% level. The A2390 cluster does not appear to alter significantly the derived number counts. However, the large Poisson error of our measurements weakens this conclusion.

6.3. Comparison to Coma Cluster Counts

Coma is a local ($z=0.0231$) cluster of galaxies, while our clusters are at redshifts of $z=0.228$ and $z=0.375$. In cluster environments, the fraction of LLRGs decreases with decreasing redshift (M99). Thus, evolution effects may be significant and no direct comparison is possible. However, we may compare our results with the Coma cluster counts merely to check for consistency given this known evolution with redshift. Specifically, our finding that $z \sim 0.3$ cluster LLRGs are not a major component in the derived number counts would be at odds with a local measurement showing a significant LLRG contribution.

Miller et al. (2009) surveyed two $\sim 0.5 \text{ deg}^2$ 1.4 GHz VLA observations covering the core and southwest region of the Coma cluster. They presented number counts from 0.110 mJy (their 5σ limit) to 100 mJy. Their counts have only been corrected for areal coverage. Thus, their faint counts ($\lesssim 0.230$ mJy) should be regarded as lower limits. At the Coma cluster's redshift LLRGs would correspond to the flux density range 16-82 mJy. No overdensity is noted in this range. Moreover, they find that their cluster counts are consistent with blank field counts (we also show this in Figure 11). The only excess of sources is in the ~ 1 -5 mJy range, and this is not attributed to a cluster effect. We conclude that our result, indicating that field galaxies make up the vast majority of sources in our cluster fields, is consistent with the local counts found in the Coma cluster field.

6.4. Gravitational Lensing Bias

Gravitational lensing affects number counts by boosting observed source flux and by magnifying the source plane. This lensing bias occurs over a relatively small area compared to our $r = 16'$ fields. Given reasonable estimates for the cluster masses and background source redshifts, we estimate that beyond 2 Mpc there is no significant lensing bias. We believe our estimate of cluster influence does not require any modifications due to lensing considerations.

6.5. Cosmic Variance

Our results are consistent with the faint number counts being primarily determined by field radio galaxies. We performed similar reduction and extraction procedures

on both cluster fields. Further, the lack of A2390 sources is already seen in the bright radio flux bins, and these should not suffer significantly from incompleteness. For these reasons, we investigate the significance of cosmic variance.

We estimate the effect of cosmic variance with the method of Somerville et al. (2004). Assuming a correlation length of 5 Mpc (consistent with the values given by Overzier et al. (2003) for NVSS mJy sources) and a redshift interval of $z = 1 \pm 0.5$, we estimate $\sim 12\%$ rms variance due to large-scale structure (see Simpson et al. 2006 for a similar calculation).

Since there is no clear consensus on the 'true' faint number counts, we choose to determine if our derived cluster number counts for the two fields can be brought into agreement given reasonable assumptions. This avoids having to develop some ad hoc method of averaging together faint number counts from radio surveys that have different analysis methods. An accurate comparison of our derived number counts depends on the accuracy of our derived error bars. While the estimated error does take into account Poisson error and the variance of our Monte Carlo simulations, it does not account for uncertainties inherent to the completeness simulations. For example, we determined a simulated object's major axis by randomly sampling from OM08's size distribution. Any inaccuracy in this distribution could alter our derived completeness corrections and thus, our derived number counts. We adopt 1.5σ error bars to account for these additional concerns. Assuming a 10% reduction in the A370 number counts to account for the cluster's influence, we find that our counts can be brought to within 1 - 2 sigma of each other. This suggests that cosmic variance can explain the disagreement seen in our derived number counts.

7. SUMMARY

We presented 1.4 GHz catalogs for the cluster fields A370 and A2390 observed with the Very Large Array. These are two of the deepest radio images of cluster fields ever taken and will be useful for both cluster and field studies. The A370 image covers an area of $40' \times 40'$ with a synthesized beam of $\sim 1.7''$ and a noise level of $\sim 5.7 \mu\text{Jy}$ near field center. The A2390 image covers an area of $\sim 34' \times 34'$ with a synthesized beam of $\sim 1.4''$ and a noise level of $\sim 5.6 \mu\text{Jy}$ near field center. We cataloged 200 redshifts for the A370 field. For the region within 16' of field center, we derived differential number counts for both fields. We found that the faint ($37 < S_{1.4 \text{ GHz}} < 3000 \mu\text{Jy}$) number counts of A370 are roughly consistent with the highest blank field counts, while the faint number counts of A2390 are roughly consistent with the lowest blank field counts. For the A370 field, we found that cluster members increase our derived number counts by $\sim 10\%$, while the A2390 cluster does not appear to contribute significantly to the presented faint number counts.

We suggest that the disagreement between our faint number counts can be primarily attributed to cosmic variance. We note that our observed fields, consisting of single pointings with nonuniform sensitivity and contaminated by foreground clusters, are not ideal to resolve definitively the debate over the importance of cosmic variance on faint radio sources. Further progress

awaits a large area survey that probes the micro-Jansky population.

We would like to thank the referee for their critical reading of the paper and useful suggestions for improving it. We gratefully acknowledge support from NSF grant AST 0708793, the University of Wisconsin Research Committee with funds granted by the Wisconsin

Alumni Research Foundation and the David and Lucile Packard Foundation (A. J. B.). Additional support was provided by a Wisconsin Space Grant Consortium Graduate Fellowship, a Sigma Xi Grant in Aid of Research, and a National Radio Astronomy Observatory Graduate Internship (I. G. B. W.). The National Radio Astronomy Observatory is a facility of the National Science Foundation operated under cooperative agreement by Associated Universities, Inc.

REFERENCES

- Alexander, D. M., Bauer, F. E., Chapman, S. C., et al. 2005, *ApJ*, 632, 736
- Appleton, P. N., Fadda, D. T., Marleau, F. R., et al. 2004, *ApJS*, 154, 147
- Baars, J. W. M., Genzel, R., Pauliny-Toth, I. I. K., & Witzel, A. 1977, *A&A*, 61, 99
- Baugh, C. M., Lacey, C. G., Frenk, C. S., et al. 2005, *MNRAS*, 356, 1191
- Barger, A. J., Cowie, L. L., Sanders, D. B., et al. 1998, *Nature*, 394, 248
- Barger, A. J., Cowie, L. L., & Sanders, D. B. 1999, *ApJ*, 518, L5
- Barger, A. J., Cowie, L. L., & Richards, E. A. 2000, *AJ*, 119, 2092
- Bower, R. G., Benson, A. J., Malbon, R., Helly, J. C., Frenk, C. S., Baugh, C. M., Cole, S., & Lacey, C. G. 2006, *MNRAS*, 370, 645
- Biggs, A. D., & Ivison, R. J. 2006, *MNRAS*, 371, 963
- Butcher, H., & Oemler, A., Jr. 1984, *ApJ*, 285, 426
- Capak, P., Carilli, C. L., Lee, N., et al. 2008, *ApJ*, 681, L53
- Capak, P. L., Riechers, D., Scoville, N. Z., et al. 2011, *Nature*, 470, 233
- Chapman, S. C., Barger, A. J., Cowie, L. L., et al. 2003, *ApJ*, 585, 57
- Chapman, S. C., Blain, A. W., Smail, I., & Ivison, R. J. 2005, *ApJ*, 622, 772
- Condon, J. J. 1989, *ApJ*, 338, 13
- Condon, J. J. 1992, *ARA&A*, 30, 575
- Condon, J. J., Cotton, W. D., Greisen, E. W., Yin, Q. F., Perley, R. A., Taylor, G. B., & Broderick, J. J. 1998, *AJ*, 115, 1693
- Condon, J. J. 2007, *Deepest Astronomical Surveys*, 380, 189
- Coppin, K. E. K., Smail, I., Alexander, D. M., et al. 2009, *MNRAS*, 395, 1905
- Coppin, K. E. K., Chapman, S. C., Smail, I., et al. 2010, *MNRAS*, 407, L103
- Cowie, L. L., Barger, A. J., & Kneib, J.-P. 2002, *AJ*, 123, 2197
- Croton, D. J., et al. 2006, *MNRAS*, 365, 11
- Daddi, E., Dannerbauer, H., Krips, M., et al. 2009a, *ApJ*, 695, L176
- Daddi, E., Dannerbauer, H., Stern, D., et al. 2009b, *ApJ*, 694, 1517
- Dannerbauer, H., Walter, F., & Morrison, G. 2008, *ApJ*, 673, L127
- Dunlop, J. S., Peacock, J. A., Savage, A., et al. 1989, *MNRAS*, 238, 1171
- Eales, S., Lilly, S., Gear, W., et al. 1999, *ApJ*, 515, 518
- Egami, E., Rex, M., Rawle, T. D., et al. 2010, *A&A*, 518, L12
- Ferrarese, L., & Merritt, D. 2000, *ApJ*, 539, L9
- Granato, G. L., De Zotti, G., Silva, L., Bressan, A., & Danese, L. 2004, *ApJ*, 600, 580
- Helou, G., Soifer, B. T., & Rowan-Robinson, M. 1985, *ApJ*, 298, L7
- Holland, W. S., Robson, E. I., Gear, W. K., et al. 1999, *MNRAS*, 303, 659
- Hopkins, P. F., Hernquist, L., Cox, T. J., et al. 2005, *ApJ*, 630, 705
- Hughes, D. H., Serjeant, S., Dunlop, J., et al. 1998, *Nature*, 394, 241
- Ibar, E., Ivison, R. J., Biggs, A. D., Lal, D. V., Best, P. N., & Green, D. A. 2009, *MNRAS*, 397, 281
- Ivison, R. J., Greve, T. R., Smail, I., et al. 2002, *MNRAS*, 337, 1
- Ivison, R. J., Magnelli, B., Ibar, E., et al. 2010, *A&A*, 518, L31
- Keenan, R. et al. 2012, *ApJ*, submitted
- Kneib, J. P., Mellier, Y., Fort, B., & Mathez, G. 1993, *A&A*, 273, 367
- Kneib, J.-P. 2002, *The Shapes of Galaxies and their Dark Halos*, 50
- Knudsen, K. K., van der Werf, P. P., & Kneib, J.-P. 2008, *MNRAS*, 384, 1611
- Knudsen, K. K., Kneib, J.-P., Richard, J., Petitpas, G., & Egami, E. 2010, *ApJ*, 709, 210
- Kormendy, J., & Richstone, D. 1995, *ARA&A*, 33, 581
- Kurtz, M. J., & Mink, D. J. 1998, *PASP*, 110, 934
- Lukić, Z., Heitmann, K., Habib, S., Bashinsky, S., & Ricker, P. M. 2007, *ApJ*, 671, 1160
- Mao, M. Y., Huynh, M. T., Norris, R. P., et al. 2011, *ApJ*, 731, 79
- Miller, N. A., Hornschemeier, A. E., & Mobasher, B. 2009, *AJ*, 137, 4436
- Morrison, G. E. 1999, Ph.D. Thesis,
- Morrison, G. E., & Owen, F. N. 2003, *AJ*, 125, 506
- Morrison, G. E., Owen, F. N., Dickinson, M., Ivison, R. J., & Ibar, E. 2010, *ApJS*, 188, 178
- Owen, F. N., & Morrison, G. E. 2008, *AJ*, 136, 1889
- Owen, F. N., Morrison, G. E., Klimek, M. D., & Greisen, E. W. 2009, *AJ*, 137, 4846
- Overzier, R. A., Röttgering, H. J. A., Rengelink, R. B., & Wilman, R. J. 2003, *A&A*, 405, 53
- Richards, E. A. 2000, *ApJ*, 533, 611
- Richard, J., Kneib, J.-P., Limousin, M., Edge, A., & Jullo, E. 2010, *MNRAS*, 402, L44
- Riechers, D. A., Capak, P. L., Carilli, C. L., et al. 2010, *ApJ*, 720, L131
- Schinnerer, E., Carilli, C. L., Capak, P., et al. 2008, *ApJ*, 689, L5
- Simpson, C., et al. 2006, *MNRAS*, 372, 741
- Smail, I., Ivison, R. J., & Blain, A. W. 1997, *ApJ*, 490, L5
- Smail, I., Morrison, G., Gray, M. E., et al. 1999, *ApJ*, 525, 609
- Somerville, R. S., Lee, K., Ferguson, H. C., Gardner, J. P., Moustakas, L. A., & Giavalisco, M. 2004, *ApJ*, 600, L171
- Tremaine, S., Gebhardt, K., Bender, R., et al. 2002, *ApJ*, 574, 740
- Wang, W.-H., Cowie, L. L., van Sadlers, J., Barger, A. J., & Williams, J. P. 2007, *ApJ*, 670, L89
- White, R. L., Becker, R. H., Helfand, D. J., & Gregg, M. D. 1997, *ApJ*, 475, 479
- White, R. L. 2008, *American Institute of Physics Conference Series*, 1082, 37